

Co₃O₄ Nanoparticle/F, N-codoped Graphene for High Efficiency Oxygen Reduction and Zinc-air Battery

Haiwei Yang,^[a] Siqing Shao,^[a, b] Wenxiang Zhu,^[a] Mengjie Ma,^[a] Yi Zhang,^[a] Chenrui Shao,^[a] Fan Liao,^[a] Ziliang Chen,^[a] Mingwang Shao,^{*[a]} and Kui Yin^{*[a, c]}

The connection between the active components and supports in a catalyst is important for the high activity and long-term stability during catalysis. Here, Co₃O₄ nanoparticles embedded in F, N-doped graphene (Co₃O₄/F, N-doped G) are synthesized by silicon-hydrogen bond reduction. F and N atoms doped graphene interacts with Co₃O₄ nanoparticles to optimize oxygen reduction reaction (ORR) catalytic activity. The optimal Co₃O₄/F, N-doped G-2 catalyst with Co loading of 3.38 wt%

shows a half-wave potential of 0.852 V vs RHE in 0.1 M KOH solution. Furthermore, Co₃O₄/F, N-doped G-2 catalyst outputs an extremely high open circuit voltage of 1.47 V and an excellent power density of 280 mW cm⁻² at current density of 450 mA cm⁻² when applied to the primary Zn-air batteries. Due to the synergistic effects from Co₃O₄ and supports (F, N-doped G), Co₃O₄/F, N-doped G-2 catalyst also shows excellent stability and anti-toxicity, and has good practical application prospects.

Introduction

The usage of fossil fuels has brought environmental pollution and serious energy crisis.^[1] With the decrease of non-renewable sources, the development of new renewable energy storage and conversion devices has become a constant goal.^[2] Fuel cell is a device with practical application value because of its advantages such as high specific energy and power generation efficiency, low environmental pollution and noise, as well as a wide range of fuel sources.^[3]

As a cathode reaction for fuel cells, oxygen reduction reaction (ORR) shows sluggish reaction kinetics in a fuel cell device.^[4] Therefore, a large number of researches focus on the development of highly efficient ORR catalysts. At present, platinum (Pt) is proved to be one of the best ORR catalysts.^[5] However, its poor reserve and expensive price severely limit the widely application. Moreover, the Pt nanoparticles in the catalysts tend to agglomerate as the reaction goes on, which seriously affects the stability of the catalysts. In addition, it has poor methanol tolerance and toxicity resistance.^[6] Therefore, it is imperative to develop ORR catalysts with low cost, high efficiency and good chemical stability to replace Pt-based catalysts.

In recent years, transition metals such as Fe, Co, Ni and their compounds have been widely studied as ORR catalysts.^[7] Among them, cobalt oxide (Co₃O₄) has become one of the most promising ORR electrocatalysts because of its abundance and excellent ORR activity.^[8] However, pure Co₃O₄ usually has low electrical conductivity and limited active site exposure.^[9] In order to fully expose the active sites and facilitate electronic transport for Co₃O₄, carbon-based materials (graphene, carbon nanotubes, carbon black, etc.) are widely used as supports for ORR catalysts.^[10] Furthermore, the charge density and electronic structure of carbon-based materials can be changed by heteroatom doping^[11], so as to regulate the chemical adsorption/desorption of the reaction intermediates to optimize the catalytic reaction activity.^[12] A large number of scientific studies have shown that the combination of Co₃O₄ and heteroatom doped carbon-based materials generates synergistic effect, which further leads to high catalytic activity.^[13] However, catalysts composed of cobalt oxide and heteroatom doped carbon-based materials usually require complex pyrolysis methods and the performances are often relied on high Co contents, which increase the manufacturing cost and time.^[14] Therefore, it is imperative to develop a simple and efficient method to synthesize Co₃O₄ nanoparticles and heteroatom doped carbon composites as efficient ORR catalysts.

In addition, to further improve the stability of the composite catalysts, the connection between catalysts and supports need to be strengthened. Dual heteroatoms doping is an effective strategy to reach this goal. Fluorine (F) element processes large electronegativity compared with other heteroatoms. It can lead to obvious charge delocalization and charge redistributions of carbon-based materials, increasing the electrical conductivity and electron transportation. The electrophilic ability of F also hinders the carbon corrosion and enhances the stability of the carbon-based composites.^[15] However, compared with other heteroatoms, F atoms are difficult to be doped into carbon-based materials in a simple way. Therefore, the corresponding studies are rarely reported.

[a] H. Yang, S. Shao, W. Zhu, M. Ma, Y. Zhang, C. Shao, Dr. F. Liao, Dr. Z. Chen, Prof. M. Shao, Dr. K. Yin
Institute of Functional Nano & Soft Materials (FUNSOM), Jiangsu Key Laboratory for Carbon-Based Functional Materials & Devices, Soochow University, 215123 Suzhou, P. R. China
E-mail: mwshao@suda.edu.cn

[b] S. Shao
School of Textile Science and Engineering, Jiangnan University, 214122 Wuxi, P. R. China

[c] Dr. K. Yin
Suzhou Weimu Intelligent System Co., Ltd.
215123, Suzhou, P. R. China
E-mail: kuiy@suda.edu.cn

 Supporting information for this article is available on the WWW under <https://doi.org/10.1002/slct.202300616>

Here, a simple way using silicon nanowires (SiNWs) and NH_4F as composite reducing agents to obtain F, N co-doped graphene as the substrate for catalysts is proposed. Due to the addition of NH_4F , element F is successfully doped into the N-doped graphene during the silicon-hydrogen (Si–H) bonds reduction process. Co_3O_4 nanoparticles are firmly embedded in F, N-doped of graphene ($\text{Co}_3\text{O}_4/\text{F}$, N-doped G) by this composite reducing agent. Due to the synergistic effects between Co_3O_4 and doped graphene, the composite catalyst has excellent ORR catalytic activity. With very low Co loading, the optimal $\text{Co}_3\text{O}_4/\text{F}$, N-doped G-2 shows a superior ORR activity with a half-wave potential of 0.852 V vs RHE, which is better than that of commercial Pt/C (0.849 V vs RHE). In addition, $\text{Co}_3\text{O}_4/\text{F}$, N-doped G-2 demonstrates good methanol tolerance and long-term stability. The current attenuation is only 7% over a long period test of up to 10 h. Furthermore, The $\text{Co}_3\text{O}_4/\text{F}$, N-doped G-2 is applied to the primary Zn-air batteries, which supplies an extremely high open circuit voltage of 1.4 V and a superior power density of 280 mW cm^{-2} at 450 mA cm^{-2} .

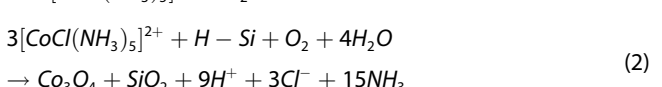
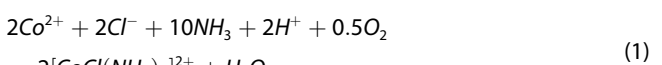
Results and Discussion

Synthesis mechanism of $\text{Co}_3\text{O}_4/\text{F}$, N-doped G

Si–H bonds reduction is often used to prepare noble metal nanoparticles in acidic systems, while the preparation of non-noble metal materials is very rare. Here, we use NH_4F and SiNWs as raw materials to reduce Co^{3+} ions under weak alkaline conditions and introduce F doping into N-doped graphene at the same time.

$\text{Co}_3\text{O}_4/\text{F}$, N-doped G is synthesized through a simple two-step process. Firstly, the catalyst support of N-doped G is prepared. Then the reduction reaction of Co^{3+} happened in the Teflon-lined stainless steel autoclave at 140 °C. The detailed preparation steps of the catalyst are shown in Scheme 1. The whole synthetic process is analyzed to explore the formation mechanism of Co_3O_4 . When NH_4F is added dropwise to CoCl_2 solution, Co^{2+} ions are oxidized into Co^{3+} and then pink precipitation $[\text{CoCl}(\text{NH}_3)_5]^{2+}$ are produced (Equation 1). Then the Co^{3+} in the precipitation is reduced by Si–H bonds to form

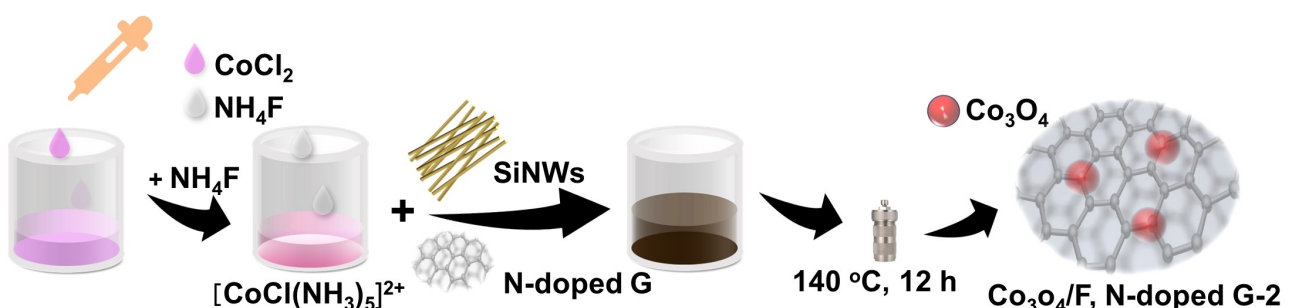
Co_3O_4 nanoparticles (Equation 2). The possible reaction equations are as follows:



Characterization for $\text{Co}_3\text{O}_4/\text{F}$, N-doped G

The crystal structure of Co_3O_4 is determined by X-ray powder diffractometer (XRD, Figure 1A and Figure S1). The peaks at 19.0°, 31.3°, 36.8°, 44.8°, 59.4° and 65.2° are corresponding to (111), (220), (311), (400), (511) and (440) crystal planes of Co_3O_4 (space group: $Fd\bar{3}\text{m}$, JCPDS card No. 43-1003),^[16] respectively. Transmission electron microscopy (TEM) images of $\text{Co}_3\text{O}_4/\text{F}$, N-doped G-2 indicates that Co_3O_4 nanoparticles are uniformly distributed on F, N-doped G (Figure 1C, 1D). According to the statistics of the exhibited nanoparticles, the average particle size of Co_3O_4 is 15 nm. High-resolution transmission electron microscopy (HRTEM) shows the lattice stripes of Co_3O_4 (Figure 1E). The lattice spacings of 0.233 nm and 0.243 nm corresponds to the (2-22) and (311) planes of cubic Co_3O_4 , with the intersection angle of 58.5°. High angle annular dark field scanning transmission electron microscopy (HAADF-STEM) image of $\text{Co}_3\text{O}_4/\text{F}$, N-doped G-2 shows the uniform distribution of Co, C, N, O and F elements, indicating that the N and F elements are doped in graphene lamellar support (Figure 1F and Figure 1G–1K). The loading amount of Co element in each catalyst is listed in Table S1. Furthermore, the TEM image of $\text{Co}_3\text{O}_4/\text{F}$, N-doped G-3 shows that increase of Co loading leads to a certain degree of agglomeration (Figure S2B), which reduces the utilization of active sites.

Further, the element composition of the $\text{Co}_3\text{O}_4/\text{F}$, N-doped G-2 is analyzed by X-ray photoelectron spectrometer (XPS). The result of XPS demonstrates the existing elements of C, N, Co, O, and F (Figure 1B). Figure S3 shows the XPS high-resolution fine spectra of C, F, N, O, and Co. The high-resolution scanning results of Co 2p are shown in Figure S3A. The peaks at 795.0 eV and 779.9 eV are attributed to Co 2p_{1/2} and Co 2p_{3/2}, respec-



Scheme 1. Schematic of the synthesis methods for $\text{Co}_3\text{O}_4/\text{F}$, N-doped G-2.

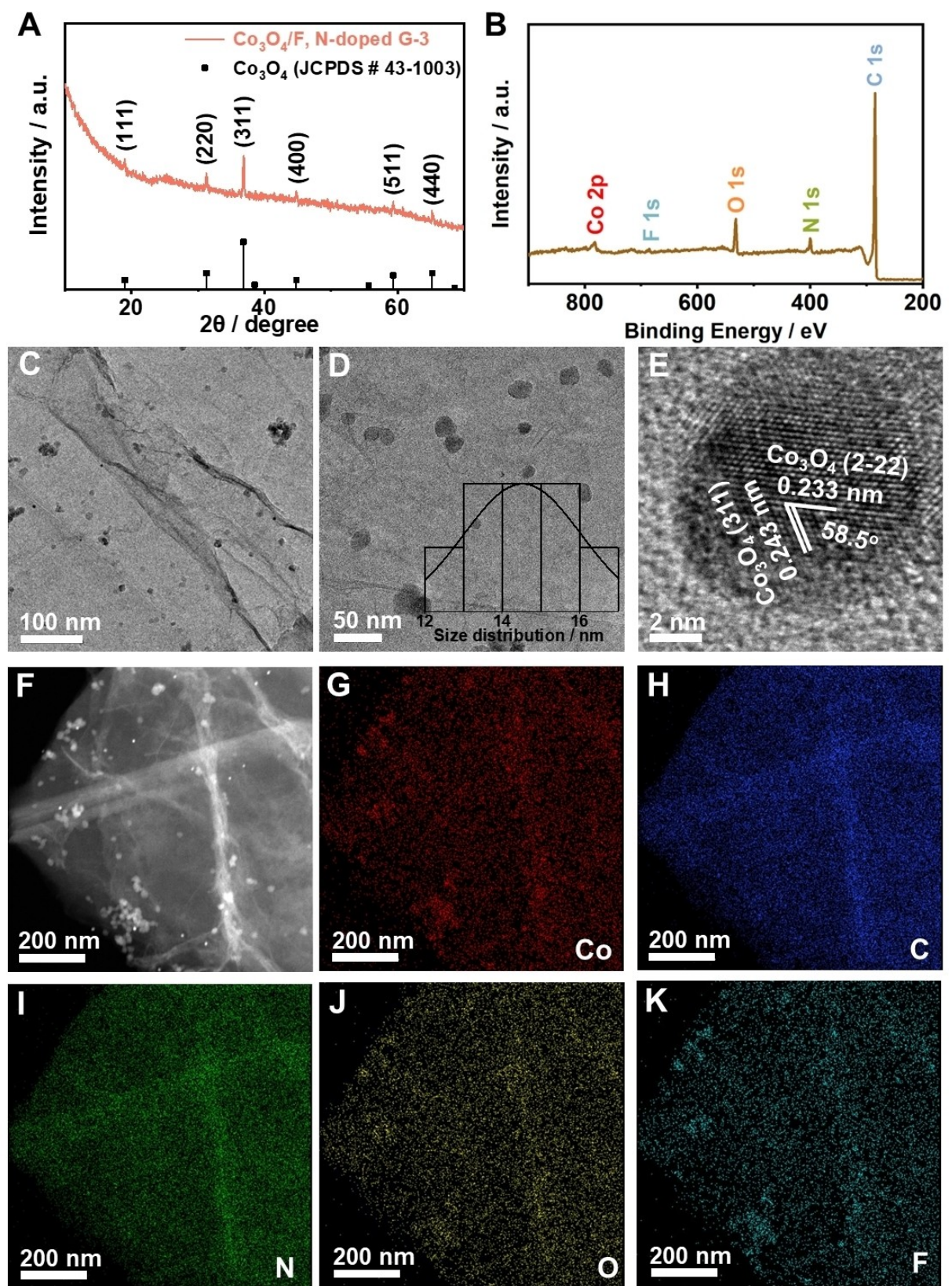


Figure 1. Characterization of $\text{Co}_3\text{O}_4/\text{F}$, N-doped G-3: (A) XRD pattern of $\text{Co}_3\text{O}_4/\text{F}$, N-doped G-3, (B) XPS full spectrum of $\text{Co}_3\text{O}_4/\text{F}$, N-doped G-2, (C) and (D) TEM images of $\text{Co}_3\text{O}_4/\text{F}$, N-doped G-2, Illustration in (D) The particle size distribution of Co_3O_4 nanoparticles obtained by TEM image, (E) HRTEM image of $\text{Co}_3\text{O}_4/\text{F}$, N-doped G-2, (F) HAADF-STEM image of $\text{Co}_3\text{O}_4/\text{F}$, N-doped G-2, and (G–K) the corresponding elemental mappings showing the distributions of Co (red), C (blue), N (green), O (yellow), and F (cyan) elements evenly.

tively, which are consistent with previously reported results, showing a separation of about 15 eV. Co 2p XPS peak of the $\text{Co}_3\text{O}_4/\text{F}$, N-doped G-2 can be deconvoluted into three types of peaks, corresponding to the Co^{3+} (794.6 eV and 779.6 eV), Co^{2+} (796.4 eV and 781.3 eV) and satellite peaks, respectively. There is a certain negative shift compared with the standard values.^[17] Furthermore, the C 1s spectrum has four resolution peaks, located at 288.4 eV, 286.7 eV, 285.7 eV and 284.5 eV, which are corresponding to semi-ionic C–F, C–O, C–N, and C=C, respectively.^[18] The N 1s spectrum (Figure S3C) can be divided into four kinds of N, corresponding to quaternary-N (401.3 eV), pyrrolic-N (400.1 eV), pyridinic-N (398.4 eV) and Co–Nx (399.1 eV).^[19] Co–Nx reveals the chemical coupling effect between Co_3O_4 and doped graphene, and N-doping further enhances the coupling between Co_3O_4 and graphene. This effect may be significant for excellent ORR reaction activity. Figure S3D shows the high-resolution O 1s peak. The peaks at 530.1 eV, 530.3 eV and 532.8 eV correspond to CoO, lattice oxygen species (O_{lat}) and water molecules that adsorbed on the sample surface (O_{abs}), respectively.^[20] F 1s spectrum (Figure S3E) has two spectral peaks at 689.0 eV and 684.7 eV, corresponding to ionic C–F and semi-ionic C–F, respectively.^[21] The successful introduction of F atoms into graphene changes the electronic structure and charge distribution of graphene, which further enhance the electron transfer and improve the conductivity and electrochemistry activity of the catalysts.

Raman spectroscopy is a favorable method to determine the layer property of sheet samples.^[22] Relevant samples are tested by Raman spectroscopy. Figure S4A shows the Raman spectrum of GO. Both G-peak and D-peak are Raman characteristic peaks of carbon, which are around 1580 cm^{-1} and 1300 cm^{-1} , respectively. D-peak represents the defect and G-peak represents the in-plane stretching vibration of C atom sp^2 hybridization. The change of the ratio of the two peaks indicates the defect of the graphene structure or the change of the doping amount. Higher ratio means that there are more defects or heteroatom doping in graphene structure.^[23] The peak intensity ratios of D to G ($I_{\text{D}}/I_{\text{G}}$) in GO, N-doped G, $\text{Co}_3\text{O}_4/\text{F}$ -doped G and $\text{Co}_3\text{O}_4/\text{F}$, N-doped G-2 are 1.04, 1.14, 1.26 and 1.29 (Figure S4), respectively. Compared with GO, the peak intensities of D and G in N-doped G increase significantly, indicating that N-doped G has more defects. In addition, the high peak strength ratio of D to G also proves that N, F atoms have been successfully doped into the graphene lamellar structure or framework which modified the structure of graphene.

ORR performance of $\text{Co}_3\text{O}_4/\text{F}$, N-doped G

The cyclic voltammetry (CV) curves of samples are tested in 0.1 M KOH solution. Figure S5 shows the CV curves of these four catalysts (N-GO, $\text{Co}_3\text{O}_4/\text{F}$ -doped GO, $\text{Co}_3\text{O}_4/\text{F}$, N-doped G-2 and commercial Pt/C) in nitrogen and oxygen saturated solutions. The four catalysts have no obvious redox peak in N_2 -saturated environment, but show obvious redox peak in oxygen environment. The oxygen reduction peak potentials at 0.660 V vs RHE and 0.781 V vs RHE correspond to N-doped G

and $\text{Co}_3\text{O}_4/\text{F}$ -doped GO, respectively. The potential of oxygen reduction peak in CV curve has an obvious guiding significance for ORR activity of the catalyst. Low positive redox peak potentials indicate poor ORR activity. The redox potential of $\text{Co}_3\text{O}_4/\text{F}$, N-doped G-2 is 0.841 V vs RHE, which is very close to the reduction peak of 0.845 V vs RHE of commercial Pt/C, indicating its outstanding ORR reactivity.

Next, the LSV curves are shown in Figure 2A, which reveal that $\text{Co}_3\text{O}_4/\text{F}$, N-doped G-2 has good ORR performance while N-doped G and $\text{Co}_3\text{O}_4/\text{F}$ -doped GO have poor activity, which may be judged from the following three aspects: (1) $\text{Co}_3\text{O}_4/\text{F}$, N-doped G-2 is the optimum sample with a positive onset potential of 0.97 V vs RHE,^[24] better than N-doped G (0.93 V vs RHE) and $\text{Co}_3\text{O}_4/\text{F}$ -doped GO (0.90 V vs RHE). This onset potential value is closed to the commercial Pt/C (0.99 V vs RHE). (2) The superior half-wave potential of $\text{Co}_3\text{O}_4/\text{F}$, N-doped G-2 is of 0.852 V vs RHE, which is almost equivalent to the commercial Pt/C of 0.849 V vs RHE, 0.170 V and 0.121 V higher those of N-doped G (0.682 V vs RHE) and $\text{Co}_3\text{O}_4/\text{F}$ -doped GO (0.731 V vs RHE), respectively. (3) The limiting current density of $\text{Co}_3\text{O}_4/\text{F}$, N-doped G-2 is 5.2 mA cm^{-2} , which is very close to 5.7 mA cm^{-2} of commercial Pt/C. The oxygen reduction current of $\text{Co}_3\text{O}_4/\text{F}$, N-doped G-2 is significantly higher than that of N-doped G and $\text{Co}_3\text{O}_4/\text{F}$ -doped GO. The ORR activity of $\text{Co}_3\text{O}_4/\text{F}$, N-doped G-2 is also compared with other advanced Co-based catalysts (Table S2), showing that $\text{Co}_3\text{O}_4/\text{F}$, N-doped G-2 has excellent half-wave potential and onset potential values.

Further, $\text{Co}_3\text{O}_4/\text{F}$, N-doped G with different Co content is compared. The CV curves of $\text{Co}_3\text{O}_4/\text{F}$, N-doped G-1 and $\text{Co}_3\text{O}_4/\text{F}$, N-doped G-3 in nitrogen and oxygen saturated environments are shown in Figure S6. They also have no obvious reduction peak in nitrogen saturated environment. In the oxygen-saturated environment, the peak potentials of positive redox are 0.80 V vs RHE and 0.78 V vs RHE respectively, which is 0.041 V and 0.061 V lower than that of $\text{Co}_3\text{O}_4/\text{F}$, N-doped G-2 in ORR activity. The LSV curves of three $\text{Co}_3\text{O}_4/\text{F}$, N-doped G samples are shown in Figure 2B. The positive onset potentials of $\text{Co}_3\text{O}_4/\text{F}$, N-doped G-1, 2 and 3 are 0.91 V vs RHE, 0.97 V vs RHE and 0.89 V vs RHE, and the half-wave potentials are 0.823 V vs RHE, 0.852 V vs RHE and 0.788 V vs RHE, respectively, indicating that $\text{Co}_3\text{O}_4/\text{F}$, N-doped G-2 is the best one among the three catalysts. The performance degradation at higher loads of Co_3O_4 can be attributed to the partial aggregation of the catalyst, which further reduces the utilization of the active center. Next, the catalytic kinetic process is studied by Tafel slope. Compared with commercial Pt/C (78 mV dec^{-1}), $\text{Co}_3\text{O}_4/\text{F}$, N-doped G-2 has a lower Tafel slope (42 mV dec^{-1}), indicating that the catalyst has better kinetic performance (Figure 2C). The Tafel slope of the remaining samples is given in the Support information (Figure S7).

The electrochemical surface area (ECSA) values greatly affect the electrochemical performance of the catalysts. The large ECSA of the catalyst usually means the high exposed active sites, which will lead to enhanced electrochemical performance. The ECSA values are calculated from the electric double layer capacitance (EDLC).^[25] A series of CV curves of the relevant catalysts are measured at a N_2 -saturated 0.1 M KOH

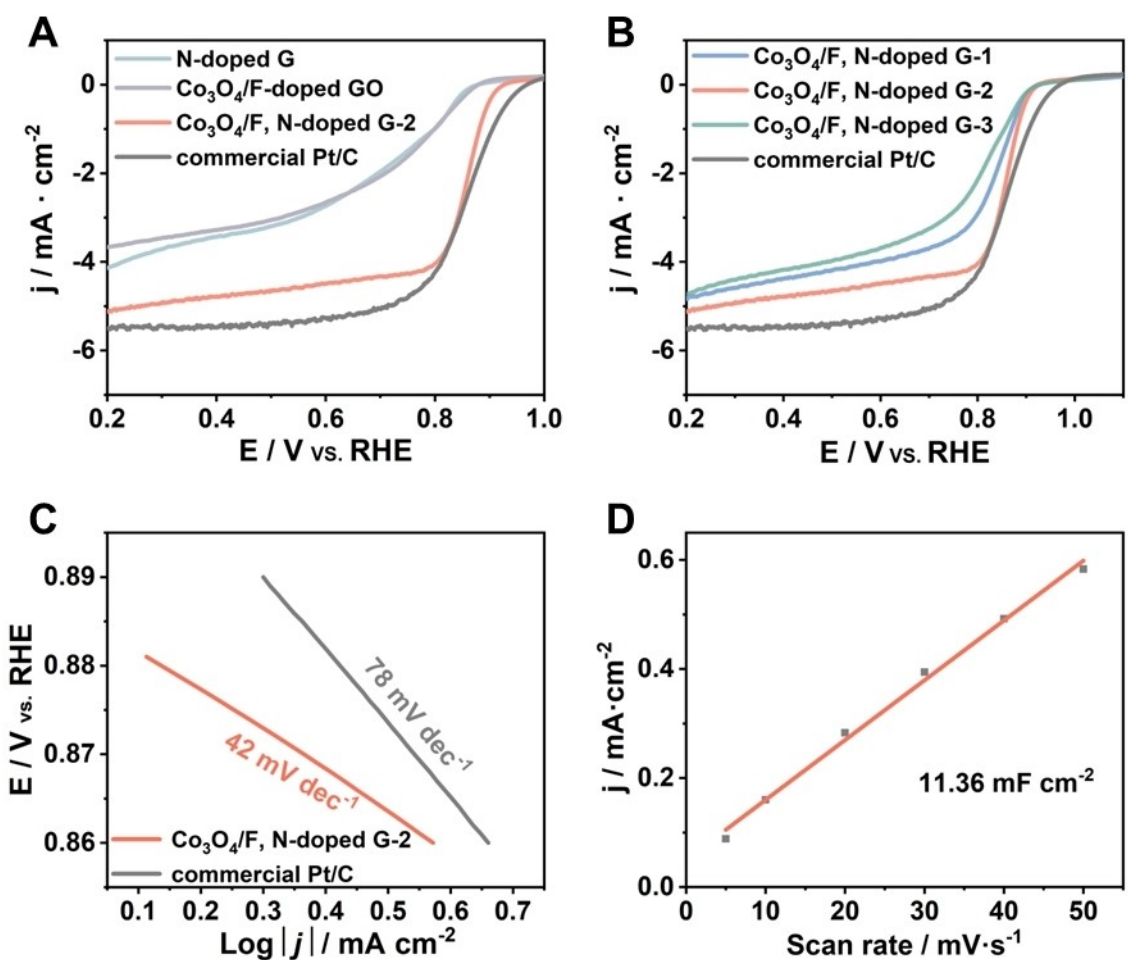


Figure 2. Electrochemical performance: (A) The LSV curves of N-doped G, Co₃O₄/F-doped GO, Co₃O₄/F, N-doped G-2 and commercial Pt/C, in 0.1 M KOH with O₂-saturated. The rotational speed was 1600 rpm. (B) The LSV curves of Co₃O₄/F, N-doped G-1, 2, 3 and commercial Pt/C (20 wt%), in 0.1 M KOH with O₂-saturated. (C) Tafel slopes of Co₃O₄/F, N-doped G-2 and the commercial Pt/C. (D) The relationship between the scanning rate and the current density when the Co₃O₄/F, N-doped G-2 was 0.92 V vs RHE.

with a voltage range of 0.87 V vs RHE to 0.97 V vs. RHE with scanning rates ranging between 5–50 mV · s⁻¹ (Figure S8–S10). The current density at a given potential shows a linear relationship with the scanning speed (Figure 2D). The EDLC of Co₃O₄/F, N-doped G-2 is measured to be 11.36 mF cm⁻², which is larger than those of Co₃O₄/F, N-doped G-1 (6.84 mF cm⁻², Figure S9) and Co₃O₄/F, N-doped G-3 (8.12 mF cm⁻², Figure S10), further confirming that Co₃O₄/F, N-doped G-2 has a large electrochemically active region and exposes more active sites during the catalysis. Specific surface area is also one of the important indicators to evaluate the activity of electrocatalysts. The specific surface area can be obtained through Brunauer–Emmett–Teller (BET) test analysis. Figure S11 shows the isothermal N₂ adsorption/desorption curves of Co₃O₄/F, N-doped G-1, 2 and 3. The BET surface area of Co₃O₄/F, N-doped G-2 (199.8 m² g⁻¹) sample is larger than that of Co₃O₄/F, N-doped G-1 (179.1 m² g⁻¹) and Co₃O₄/F, N-doped G-3 (137.7 m² g⁻¹), indicating that Co₃O₄/F, N-doped G-2 has more active sites.

In order to further understand the ORR reaction kinetics of the prepared samples, the LSV curves of the samples at

different rotational speeds are measured under the O₂-saturated electrolyte to calculate the electron transfer number. The diffusion rate of oxygen in 0.1 M KOH solution increases with the increase of the rotating speed of the disk electrode. Thus, the time of oxygen flowing to the catalyst surface is shortened, and the limiting current density obtained on the working electrode is increased. The number of electrons transferred in ORR reaction can be calculated by the Koutechy-Levich equation (Equation 3):

$$\frac{1}{j} = \frac{1}{j_k} + \frac{1}{j_D} = -\frac{1}{nFkC_{O_2}^b} - \frac{1}{0.62nFD_{O_2}^{2/3}v^{-1/6}C_{O_2}^b\omega^{1/2}} \quad (3)$$

Figure 3A shows the LSV curves of Co₃O₄/F, N-doped G-2 at different rotating speeds, by which the transfer electron number is calculated to be 3.89 (Figure 3B), indicating that the ORR reaction pathway on the Co₃O₄/F, N-doped G-2 catalyst is mainly the 4-electron process, similar to the process on the commercial Pt/C (3.96) (Figure S12). Poor ORR reactivity often means that fewer 4-electron processes are involved in the

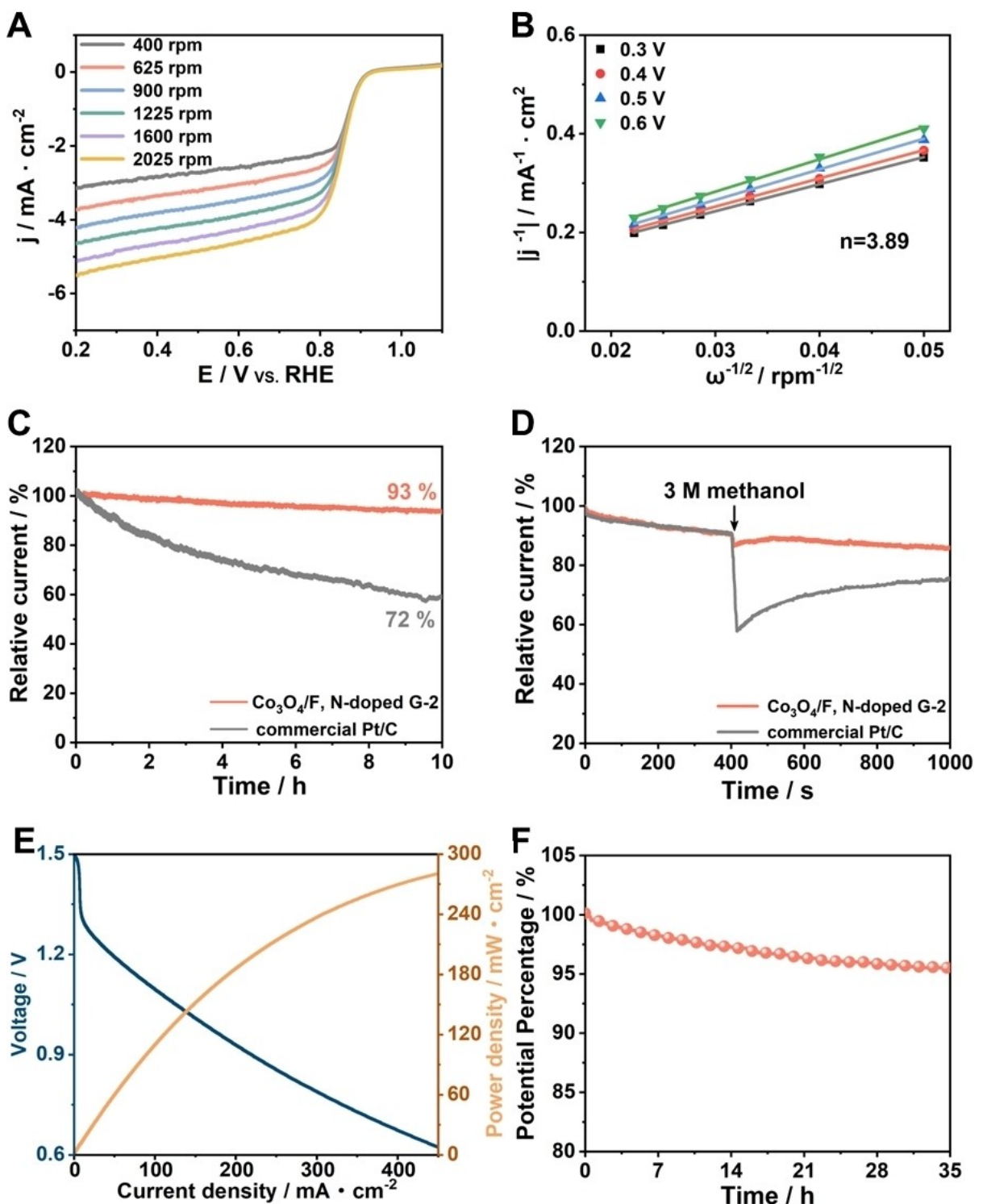


Figure 3. (A) LSV curves at different rotation speeds for $\text{Co}_3\text{O}_4/\text{F}$, N-doped G-2 in O_2 -saturation of 0.1 M KOH; and (B) K-L fitting diagrams of $\text{Co}_3\text{O}_4/\text{F}$, N-doped G-2 at different potentials and their corresponding transferred electron numbers; (C) The $i-t$ curves of $\text{Co}_3\text{O}_4/\text{F}$, N-doped G-2 and commercial Pt/C at 0.7 V vs RHE; (D) Chronoamperometric response of $\text{Co}_3\text{O}_4/\text{F}$, N-doped G-2 and commercial Pt/C at 0.7 V vs RHE in 25 mL 0.1 M KOH with addition of 2 mL 3 M CH_3OH at 400 s; (E) The power density and discharge polarization curves of Zn-air battery assembled with $\text{Co}_3\text{O}_4/\text{F}$, N-doped G-2; and (F) constant discharge curve of $\text{Co}_3\text{O}_4/\text{F}$, N-doped G-2 at 10 $\text{mA} \cdot \text{cm}^{-2}$.

reaction pathway. Compared with $\text{Co}_3\text{O}_4/\text{F}$, N-doped G-2, the transfer electron numbers of $\text{Co}_3\text{O}_4/\text{F}$, N-doped G-1 and $\text{Co}_3\text{O}_4/\text{F}$, N-doped G-3 are 3.83 and 3.85 (Figure S13 and S14), respectively. Furthermore, electrochemical impedance spectro-

scopy (EIS) results show that the transfer electron numbers of $\text{Co}_3\text{O}_4/\text{F}$, N-doped G-2, G-1, and G-3 are 3.83, 3.85, 3.83, and 3.85, respectively. The transfer electron number of $\text{Co}_3\text{O}_4/\text{F}$, N-doped G-2 is higher than that of commercial Pt/C (3.83 vs. 3.80), which is attributed to the high specific surface area and the presence of nitrogen atoms in the carbon support.

scopy (EIS) is used to reveal the charge transfer resistance between the corresponding catalysts. The electrochemical impedance spectra of $\text{Co}_3\text{O}_4/\text{F}$, N-doped G catalysts and the corresponding equivalent circuit model are shown in Figure S15 and S16. CPE_{dl} represents double-layer capacitance, CPE_{f} represents Warburg impedance, R_{f} represents intrinsic resistance of the catalyst, R_{ct} represents charge transfer resistance between electrode surface during ORR and electrolyte, and R_{s} stands represents electrolyte resistance.^[26] It can be clearly seen that the $\text{Co}_3\text{O}_4/\text{F}$, N-doped G-2 has lower charge transfer resistance than the other two, indicating its fast electron transfer process.

Electrochemical stability and methanol tolerance are also important parameters to assess the ORR performance of the catalyst. The stability of $\text{Co}_3\text{O}_4/\text{F}$, N-doped G-2 and the commercial Pt/C is measured by chronoamperometric ($i-t$) at 0.7 V vs RHE. After up to 10 hours of testing, the current of the prepared $\text{Co}_3\text{O}_4/\text{F}$, N-doped G-2 attenuate by only 7% (Figure 3C), while that of the commercial Pt/C attenuate by 28%, indicating that $\text{Co}_3\text{O}_4/\text{F}$, N-doped G-2 possesses excellent stability. This also benefits from the synergistic coupling effect between Co_3O_4 and the support (F, N-doped G), which further enhances the connection between the active components of the catalyst and the support. After the long-term stability test, the structure and morphology of $\text{Co}_3\text{O}_4/\text{F}$, N-doped G-2 is characterized. As shown in Figure S17, after the stability test, the crystal structure of Co_3O_4 has not changed, indicating that it has good stability in the ORR reaction process. The TEM image after stability test shows that the size of Co_3O_4 nanoparticles does not change significantly, and still has good dispersion (Figure S18A). The TEM-EDX mapping images also show the uniform distribution of Co, C, N, O and F elements (Figure S18B-F). After the stability test, the XPS spectrum of Co is shown in Figures S19, which demonstrated that the valence state of Co was not changed. In the anti-methanol toxicity test, $\text{Co}_3\text{O}_4/\text{F}$, N-doped G-2 showed excellent tolerance to methanol toxicity (Figure 3D). When 2 mL 3 M methanol was added to 25 mL 0.1 M KOH with O_2 -saturated, its current attenuation rate was only 3%, much better than that of the commercial Pt/C. Good methanol tolerance is exceedingly significant for commercial application. The results show that $\text{Co}_3\text{O}_4/\text{F}$, N-doped G-2 has a good application prospect.

In order to verify the practical application value of the catalyst, $\text{Co}_3\text{O}_4/\text{F}$, N-doped G-2 is prepared as an air cathode catalyst and assembled into a primary Zn-air battery. The catalyst is loaded on a hydrophobic carbon cloth, with zinc as anode and 6 M KOH solution as electrolyte. The $\text{Co}_3\text{O}_4/\text{F}$, N-doped G-2 cathode catalyst displays an extremely high open-circuit voltage of 1.47 V (Figure S20A) and an excellent peak power of 280 mW cm^{-2} at the current density of 450 mA cm^{-2} (Figure 3E), which shows better commercial values than the commercial Pt/C (Figure S20B). $\text{Co}_3\text{O}_4/\text{F}$, N-doped G-2 also exhibits superior stability in the long-term constant discharge process at 10 mA cm^{-2} (Figure 3F), demonstrating its superior application prospect.

ORR catalytic mechanism analysis of $\text{Co}_3\text{O}_4/\text{F}$, N-doped G

The above test results show that $\text{Co}_3\text{O}_4/\text{F}$, N-doped G-2 has excellent ORR activity and long-time working stability. Here, it is necessary to further reveal the underlying reasons for the highly effective ORR activity of $\text{Co}_3\text{O}_4/\text{F}$, N-doped G-2. First of all, we prepared $\text{Co}_3\text{O}_4/\text{F}$ -doped G by using graphene instead of N-doped G as the carrier of the composite catalyst, using the same synthesis process, and tested its ORR activity. As shown in Figure S21, compared with $\text{Co}_3\text{O}_4/\text{F}$, N-doped G-2, $\text{Co}_3\text{O}_4/\text{F}$ -doped G has poor ORR activity, indicating that the introduction of N element is essential for the excellent ORR activity of the composite catalyst. At the same time, we also test the performance of physical mixing of Co_3O_4 and N-doped G ($\text{Co}_3\text{O}_4 + \text{N-doped G mixture}$), and compare it with $\text{Co}_3\text{O}_4 + \text{F}$, N-doped G mixture (Figure S22). It was found that the presence of F atom promotes the conductivity of the catalyst, expands the limit current density of ORR reaction, thus further confirms the importance of double doping. Then, compared with the binding energy of Co in pure Co_3O_4 , the binding energy of Co in $\text{Co}_3\text{O}_4/\text{F}$, N-doped G-2 shows a negative shift (Figure S23), indicates that Co in $\text{Co}_3\text{O}_4/\text{F}$, N-doped G-2 catalyst is electron deficient and the existence of electron transfer from Co_3O_4 nanoparticles to N, F atoms, which can greatly affect the adsorption energy of intermediate products during ORR and further optimize the ORR activity.^[27] In order to further clarify the substantial contribution of this coupling effect to the ORR activity of the composite catalyst, we mix Co_3O_4 with F, N-doped G physically ($\text{Co}_3\text{O}_4 + \text{F}$, N-doped G mixture) and test its ORR activity. The results show that the ORR activity provided by the mixture is much lower than that of the composite (Figure S22). Therefore, the synergistic effects between Co_3O_4 and doped graphene is essential for the superior performance of the composite.

Conclusion

Co_3O_4 shows electrochemical activity and stability in alkaline electrolytes. However, the electrochemical activity is limited due to its electronic structure and exposed active sites. In this work, F, N-codoped graphene is employed as substrate to provide high electronic transportation. Due to the unique synthesis method, Co_3O_4 nanoparticles are firmly connected with F, N-codoped graphene by electron transfer, leading to outstanding catalytic activity and stability for ORR. The optimal sample $\text{Co}_3\text{O}_4/\text{F}$, N-doped G-2 shows good ORR activity with the transfer electron number of 3.89. The excellent half-wave potential of $\text{Co}_3\text{O}_4/\text{F}$, N-doped G-2 is 0.852 V vs. RHE. In addition, unlike the low methanol tolerance of the commercial Pt/C, $\text{Co}_3\text{O}_4/\text{F}$, N-doped G-2 exhibits excellent stability over a long period of operation. Further, the $\text{Co}_3\text{O}_4/\text{F}$, N-doped G-2 cathode catalyst is used to assemble the primary Zn-air battery, and shows excellent practical application value. This work provides a new idea for the preparation of ORR catalysts to replace Pt-based precious metals.

Experimental Section

Materials

Cobalt chloride hexahydrate ($\text{CoCl}_2 \cdot 6\text{H}_2\text{O}$), ammonium fluoride (NH_4F), glycol ($(\text{CH}_2\text{OH})_2$), ammonia ($\text{NH}_3 \cdot \text{H}_2\text{O}$, 30%) and hydrazine hydrate (N_2H_4 , 85%) were purchased from Sinopharm Chemical Reagent Co. Ltd. Graphene oxide (GO) was supplied by Nanjing Xianfeng nanomaterial Company. The commercial Pt/C catalysts with Pt content of 20 wt% were purchased from Alfa Aesar Chemical Co. Ltd. Other materials were analytical reagent grade. Holey carbon support films (Zhongjingkeyi (Beijing) Film Technology Co., Ltd) were used to support the materials. All aqueous solutions in the whole experiment were prepared with double distilled water.

Synthesis of N-doped graphene (N-doped G)

N-doped G was synthesized using the purchased graphene oxide (GO) as the raw material according to the previous work.^[28] In details, 30 mg GO was dispersed into 30 mL ultra-pure water and ultrasounded to form the GO aqueous dispersion. $\text{NH}_3 \cdot \text{H}_2\text{O}$ was employed to adjust the pH value to 10. Then 0.6 mL N_2H_4 was added to the mixture and stirred for 10 min. Then, the mixture was transferred into a Teflon-lined autoclave and heated at 180 °C for 3 hours. Rinse the product three times with ultra-pure water and dry it in a freeze dryer for 24 hours.

Synthesis of $\text{Co}_3\text{O}_4/\text{F}$, N-doped G-1, 2, 3 and $\text{Co}_3\text{O}_4/\text{F}$ -doped GO

First, 0.5 mL of CoCl_2 solution (0.1 M) was mixed with 3 mL of NH_4F aqueous solution (40 wt%) and stirred for 30 min as Solution A. The color of the solution became pink, indicating the formation of $[\text{CoCl}(\text{NH}_3)_5]^{2+}$. Silicon nanowires (SiNWs) were obtained by the thermal evaporative oxide-assisted growth method.^[29] Then, 5 mg SiNWs and 5 mg N-doped G and were dispersed into 10 mL of glycol solution and ultrasounded for 8 h, which were then added to the Solution A. Next, the mixture was transferred into a Teflon-lined stainless steel autoclave and maintained at 140 °C for 12 h. In the whole reaction process, silicon nanowires first react with NH_4F to convert into Si–H bond. Si–H bond reduces Co^{3+} and then oxidized to SiO_2 . SiO_2 can further react with excessive NH_4F to generate SiF_4 , which is volatilized and removed after the Teflon-lined stainless steel autoclave is opened. Partial hydrolysis products of SiF_4 are soluble in water and can be removed in the subsequent sample washing process.^[30] The product was collected by washing and freeze drying and denoted as $\text{Co}_3\text{O}_4/\text{F}$, N-doped G-2. Moreover, $\text{Co}_3\text{O}_4/\text{F}$, N-doped G-1 and 3 was synthesized by different addition amounts of CoCl_2 with same other condition. $\text{Co}_3\text{O}_4/\text{F}$ -doped GO was synthesized by replacing N-doped G with GO, while other process was the same as $\text{Co}_3\text{O}_4/\text{F}$, N-doped G-2.

Synthesis of $\text{Co}_3\text{O}_4/\text{F}$ -doped G

First, 0.5 mL of CoCl_2 solution (0.1 M) was mixed with 3 mL of NH_4F aqueous solution (40 wt%) and stirred for 30 min as Solution A. The color of the solution became pink, indicating the formation of $[\text{CoCl}(\text{NH}_3)_5]^{2+}$. Then, 5 mg SiNWs and 5 mg graphene and were dispersed into 10 mL of glycol solution and ultrasounded for 8 h, which were then added to the Solution A. Next, the mixture was transferred into a Teflon-lined stainless steel autoclave and

maintained at 140 °C for 12 h. The product was collected by washing and freeze drying and denoted as $\text{Co}_3\text{O}_4/\text{F}$ -doped G.

Characterization

The phase and crystallography of the catalysts were characterized by X-ray powder diffraction (XRD, Philips X' pert PRO MPD diffractometer) with a $\text{Cu K}\alpha$ radiation source ($\lambda = 0.15406$ nm). Transmission electron microscopy (TEM), high resolution TEM (HRTEM), high angle annular dark field scanning transmission electron microscopy (HAADF-STEM) and elemental mapping by energy-dispersive X-ray spectrometry (EDS) were conducted using a FEI Tecnai F20 transmission electron microscope with an accelerating voltage of 200 kV. The chemical states of the catalysts were studied using X-ray photoelectron spectroscopy (XPS) on a Kratos AXIS UltraDLD ultrahigh vacuum surface analysis system with $\text{Al K}\alpha$ radiation (1486 eV) as a probe and an indium plate as the sample holder. Raman spectra were measured with an HR 800 Raman spectroscopy (J Y, France) equipped with a synapse CCD detector and a confocal Olympus microscope. The wavelength of the laser is 633 nm. The Co content loaded in the synthesized $\text{Co}_3\text{O}_4/\text{F}$, N-doped G heterostructure was analyzed by inductively coupled plasma (ICP) instrument.

Electrochemical measurements

All electrochemical experiments were performed by using a CHI 760 D electrochemical workstation with a three-electrode system. The working electrode was a modified glass carbon electrode (GCE, 3 mm in diameter). An Ag/AgCl electrode was employed as the reference electrode in alkaline solution and a carbon rod was used as the counter electrode. To prepare the working electrode, 2.0 mg catalysts were dispersed in a mixed solution including 0.375 mL water, 0.075 mL isopropanol and 0.05 mL Nafion solution (0.5 wt%) to form a homogeneous suspension by ultrasound. Then, 8.0 μL of the suspension was loaded on the GCE, dried naturally and conducted electrochemical test. All the experiments were tested in 25 mL 0.1 M KOH solution.

Measurement for Zn-air batteries

First, 48 μL $\text{Co}_3\text{O}_4/\text{F}$, N-doped G-2 suspension was dropped on carbon cloth to fabricate the air cathode. Commercial Pt/C was used as a comparison to prepare the cathode by the same method. Then, the prepared air cathode, commercial zinc foil as anode and 6 M KOH water solution as electrolyte were used to assemble the Zn-air batteries. Linear sweep voltammetry (LSV) curves of Zn-air batteries loaded with $\text{Co}_3\text{O}_4/\text{F}$, N-doped G-2 or commercial Pt/C were measured with a scan rate of 10 mV s^{-1} , respectively.

Supporting Information Summary

Supporting information contains some structural characterizations and electrochemical measurements. Additional references cited within the Supporting Information.^[31–39]

Acknowledgements

The project was supported by National MCF Energy R&D Program (2018YFE0306105), National Natural Science Foundation of China (51902217), Natural Science Foundation of Jiangsu Province

(BK20210735), Natural Science Foundation of the Higher Education Institutions of Jiangsu Province (21KJB430043), Collaborative Innovation Center of Suzhou Nano Science & Technology, the Priority Academic Program Development of Jiangsu Higher Education Institutions (PAPD), the 111 Project, Joint International Research Laboratory of Carbon-Based Functional Materials and Devices.

Conflict of Interests

The authors declare no conflict of interest.

Data Availability Statement

The data that support the findings of this study are available from the corresponding author upon reasonable request.

Keywords: Co₃O₄ nanoparticles • Doping • Graphene • Oxygen reduction reaction • Silicon nanowires

- [1] a) T. R. Cook, D. K. Dogutan, S. Y. Reece, Y. Surendranath, T. S. Teets, D. G. Nocera, *Chem. Rev.* **2010**, *110*, 6474–6502; b) A. I. Hochbaum, P. Yang, *Chem. Rev.* **2010**, *110*, 527–546.
- [2] X. F. He, X. Y. Long, P. Wang, H. J. Wu, P. F. Han, Y. Tang, K. K. Li, X. R. Ma, Y. T. Zhang, *J. Alloys Compd.* **2021**, *855*, 157422.
- [3] a) I. Staffell, D. Scaman, A. V. Abad, P. Balcombe, P. E. Dodds, P. Ekins, N. Shah, K. R. Ward, *Energy Environ. Sci.* **2019**, *12*, 463–491; b) X. F. Lu, Y. Chen, S. B. Wang, S. Y. Gao, X. W. Lou, *Adv. Mater.* **2019**, *31*, 1902339.
- [4] J. N. Chen, Z. Y. Wang, J. J. Mao, C. Liu, Y. Chen, Z. G. Lu, S. P. Feng, *J. Alloys Compd.* **2021**, *856*, 157379.
- [5] a) Y. W. Shen, D. C. Shi, L. B. Liu, F. Liao, W. X. Zhu, M. W. Shao, *ACS Sustainable Chem. Eng.* **2019**, *7*, 12281–12287; b) C. Guan, A. Sumboja, H. J. Wu, W. N. Ren, X. M. Liu, H. Zhang, Z. L. Liu, C. W. Cheng, S. J. Pennycook, J. Wang, *Adv. Mater.* **2017**, *29*, 1704117; c) N. G. Wang, W. P. Li, J. W. Liang, Y. X. Huang, Q. Cai, M. C. Hu, Y. Y. Chen, Z. C. Shi, *J. Alloys Compd.* **2020**, *846*, 156396.
- [6] a) A. S. Wang, C. N. Zhao, M. Yu, W. C. Wang, *Appl. Catal. B* **2021**, *281*, 119514; b) Z. H. Cai, S. X. Lin, J. J. Xiao, T. Muhammed, X. B. Hu, *Adv. Mater. Interfaces* **2021**, *8*, 2001922; c) Y. L. Wu, Y. M. Wang, Z. X. Xiao, M. T. Li, Y. L. Ding, M. L. Qi, *RSC Adv.* **2021**, *11*, 2693–2700; d) J. S. Liu, H. Zhang, J. S. Meng, C. H. Han, F. Liu, X. Liu, P. J. Wu, Z. A. Liu, X. P. Wang, L. Q. Mai, *Adv. Mater. Interfaces* **2020**, *12*, 54545–54552.
- [7] a) D. Wang, X. Pan, P. Yang, R. Li, H. Xu, Y. Li, F. Meng, J. Zhang, M. An, *ChemSusChem* **2021**, *14*, 33–55; b) D. Q. Dong, X. Y. Guo, C. L. Ma, L. Y. Gong, L. H. Su, T. Xie, Y. Zhu, J. Wang, *Mater. Today Commun.* **2020**, *24*, 101127.
- [8] a) Y. Y. Liang, Y. G. Li, H. L. Wang, J. G. Zhou, J. Wang, T. Regier, H. J. Dai, *Nat. Mater.* **2011**, *10*, 780–786; b) W. L. Zhang, S. C. Yang, S. T. Bai, L. H. Zhang, Y. K. Zhang, F. S. Yu, *ChemCatChem* **2021**, *13*, 1546–1551; c) S. J. Kim, J. H. Hong, J. K. Lee, Y. C. Kang, *J. Mater. Chem. A* **2021**, *9*, 25160–25167; d) X. Y. Yao, X. Y. Wang, L. X. Sun, L. Li, E. J. Kan, B. Ouyang, W. M. Zhang, *Inorg. Chem. Front.* **2022**, *9*, 2517–2529.
- [9] a) Y. Liu, T. Zhang, Y. E. Duan, X. Dai, Q. Tan, Y. Z. Chen, Y. N. Liu, *J. Colloid Interface Sci.* **2021**, *604*, 746–756; b) B. S. Tang, J. Yang, Z. K. Kou, L. Xu, H. L. Seng, Y. N. Xie, A. D. Handoko, X. X. Liu, Z. W. Seh, H. Kawai, H. Gong, W. F. Yang, *Energy Storage Mater.* **2019**, *23*, 1–7; c) Z. X. Huang, X. P. Qin, G. Z. Li, W. C. Yao, J. Liu, N. G. Wang, K. Ithisuphalap, G. Wu, M. H. Shao, Z. C. Shi, *ACS Appl. Energ. Mater.* **2019**, *2*, 4428–4438.
- [10] a) J. Y. Du, G. Wu, K. Liang, J. Yang, Y. D. Zhang, Y. Lin, X. S. Zheng, Z. Q. Yu, Y. Wu, X. Hong, *Small* **2021**, *17*, 2007264; b) J. Wang, F. Xu, H. Y. Jin, Y. Q. Chen, Y. Wang, *Adv. Mater.* **2017**, *29*, 1–13; c) Z. W. Seh, J. Kibsgaard, C. F. Dickens, I. B. Chorkendorff, J. K. Norskov, T. F. Jaramillo, *Science* **2017**, *355*, eaad4998.
- [11] a) F. Liu, X. Q. Zhang, X. L. Zhang, L. L. Wang, M. M. Liu, J. J. Zhang, *J. Colloid Interface Sci.* **2021**, *581*, 523–532; b) W. L. Zhang, H. X. Sun, Z. Q. Zhu, R. Jiao, P. Mu, W. D. Liang, A. Li, *Renewable Energy* **2020**, *146*, 2270–2280; c) W. J. Qi, J. T. Niu, Z. H. Huang, Z. M. Chen, X. Chen, F. Chen, F. Y. Tuo, *Int. J. Hydrogen Energy* **2020**, *45*, 521–530; d) L. Han, X. Y. Cui, Y. Y. Liu, G. S. Han, X. L. Wu, C. B. Xu, B. J. Li, *Sustain. Energy Fuels* **2020**, *4*, 2707–2717.
- [12] a) L. J. Yang, J. L. Shui, L. Du, Y. Y. Shao, J. Liu, L. M. Dai, Z. Hu, *Adv. Mater.* **2019**, *31*, 1804799; b) C. G. Hu, L. M. Dai, *Adv. Mater.* **2019**, *31*, 1804672.
- [13] a) Y. Liu, T. Zhang, Y. E. Duan, X. Dai, Q. Tan, Y. Z. Chen, Y. N. Liu, *J. Colloid Interface Sci.* **2021**, *604*, 746–756; b) Y. L. Wang, R. H. Gan, Z. Q. Ai, H. Liu, C. B. Wei, Y. Song, M. Dirican, X. W. Zhang, C. Ma, J. L. Shi, *Carbon* **2021**, *181*, 87–98; c) H. F. Peng, W. L. Zhang, Y. Song, F. X. Yin, C. W. Zhang, L. Zhang, *Catal. Today* **2020**, *355*, 286–294.
- [14] a) D. X. Ji, L. Fan, L. Tao, Y. J. Sun, M. G. Li, G. R. Yang, T. Q. Tran, S. Ramakrishna, S. J. Guo, *Angew. Chem. Int. Ed.* **2019**, *58*, 13840–13844; *Angew. Chem.* **2019**, *131*, 13978–13982; b) C. C. Wang, K. Y. Hung, T. E. Ko, S. Hosseini, Y. Y. Li, *J. Power Sources* **2020**, *452*, 227841; c) Y. G. Liu, H. Z. Zhang, N. Jiang, W. X. Zhang, H. Arandiyan, Z. Y. Wang, S. H. Luo, F. Fang, H. Y. Sun, *J. Alloys Compd.* **2020**, *834*, 155030; d) T. Singh, C. Das, N. Bothra, N. Sikdar, S. Das, S. K. Pati, T. K. Maji, *Inorg. Chem.* **2020**, *59*, 3160–3170.
- [15] a) W. Shen, L. Ge, Y. Y. Sun, F. Liao, L. Xu, Q. Dang, Z. H. Kang, M. W. Shao, *ACS Appl. Mater. Interfaces* **2018**, *10*, 33153–33161; b) Z. C. Wang, W. J. Xu, X. K. Chen, Y. H. Peng, Y. Y. Song, C. X. Lv, H. L. Liu, J. W. Sun, D. Yuan, X. Y. Li, X. X. Guo, D. J. Yang, L. X. Zhang, *Adv. Funct. Mater.* **2019**, *29*, 1902875.
- [16] W. Shen, L. Ge, Y. Sun, F. Liao, L. Xu, Q. Dang, Z. Kang, M. Shao, *ACS Appl. Mater. Interfaces* **2018**, *10*, 33153–33161.
- [17] M. Sheng, B. Jiang, B. Wu, F. Liao, X. Fan, H. Lin, Y. Li, Y. Lifshitz, S. Lee, M. Shao, *ACS Nano* **2019**, *13*, 2786–2794.
- [18] W. Hu, Y. Wang, X. Hu, Y. Zhou, S. Chen, *J. Mater. Chem.* **2012**, *22*, 6010–6016.
- [19] a) J. Feng, F. Lv, W. Zhang, P. Li, K. Wang, C. Yang, B. Wang, Y. Yang, J. Zhou, F. Lin, G. Wang, S. Guo, *Adv. Mater.* **2017**, *29*, 1703798; b) S. Freakley, J. Ruiz-Esquius, D. Morgan, *Surf. Interface Anal.* **2017**, *49*, 794–799; c) W. Xia, J. Yang, C. Liang, *Appl. Surf. Sci.* **2014**, *293*, 293–298.
- [20] a) S. Hao, J. Wen, X. Yu, W. Chu, *Appl. Surf. Sci.* **2013**, *264*, 433–442; b) J. Bejar, L. Alvarez-Contreras, M. Guerra-Balcazar, J. Ledesma-Garcia, L. Arriaga, N. Arjona, *Appl. Surf. Sci.* **2020**, *509*, 144898.
- [21] a) Y. Roginskaya, O. Morozova, E. Lubnin, Y. Ulitina, G. Lopukhova, S. Trasatti, *Langmuir* **1997**, *13*, 4621–4627; b) J. Bao, X. Zhang, B. Fan, J. Zhang, M. Zhou, W. Yang, X. Hu, H. Wang, B. Pan, Y. Xie, *Angew. Chem. Int. Ed.* **2015**, *54*, 7399–7404; *Angew. Chem.* **2015**, *127*, 7507–7512.
- [22] I. Man, H. Su, F. Calle-Vallejo, H. Hansen, J. Martinez, N. Inoglu, J. Kitchin, T. Jaramillo, J. Norskov, J. Rossmeisl, *ChemCatChem* **2011**, *3*, 1159–1165.
- [23] a) J. Rossmeisl, Z. Qu, H. Zhu, G. Kroes, J. Norskov, *J. Electroanal. Chem.* **2007**, *607*, 83–89; b) W. Cao, Y. Xu, Z. Wang, J. Luo, M. Khan, L. Zhang, D. Ye, H. Zhao, J. Zhang, *J. Electrochem. Soc.* **2020**, *167*, 104511.
- [24] O. Diaz-Morales, S. Raajiman, R. Kortlever, P. Kooyman, T. Wezendonk, J. Gascon, W. Fu, M. Koper, *Nat. Commun.* **2016**, *7*, 12363.
- [25] N. Danilovic, R. Subbaraman, K. Chang, S. Chang, Y. Kang, J. Snyder, A. Paulikas, D. Strmcnik, Y. Kim, D. Myers, V. Stamenkovic, N. Markovic, *J. Phys. Chem. Lett.* **2014**, *5*, 2474–2478.
- [26] O. Kasian, J. Grote, S. Geiger, S. Cherevko, K. Mayrhofer, *Angew. Chem. Int. Ed.* **2018**, *57*, 2488–2491; *Angew. Chem.* **2018**, *130*, 2514–2517.
- [27] a) Y. Liu, T. Zhang, Y. E. Duan, X. Dai, Q. Tan, Y. Z. Chen, Y. N. Liu, *J. Colloid Interface Sci.* **2021**, *604*, 746–756; b) T. Li, O. Kasian, S. Cherevko, S. Zhang, S. Geiger, C. Scheu, P. Felfer, D. Raabe, B. Gault, K. Mayrhofer, *Nat. Catal.* **2018**, *1*, 300–305.
- [28] Heggen, V. Petkov, R. Schlogl, T. Jones, P. Strasser, *Nat. Catal.* **2018**, *1*, 841–851.
- [29] R. Jansonius, P. Schauer, D. Dvorak, B. Macleod, D. Fork, C. Berlinguet, *Angew. Chem. Int. Ed.* **2020**, *59*, 12192–12198; *Angew. Chem.* **2020**, *132*, 12290–12296.
- [30] P. G. Sennikov, S. K. Ignatov, O. Schrems, *Russ. J. Inorg. Chem.* **2010**, *55*, 413–420.
- [31] H. Y. Yang, Z. H. Tang, K. Wang, W. Wu, Y. H. Chen, Z. Q. Ding, Z. Liu, S. W. Chen, *J. Colloid Interface Sci.* **2018**, *528*, 18–26.
- [32] G. Cheng, G. L. Liu, P. Liu, L. Y. Chen, S. B. Han, J. X. Han, F. Ye, W. Song, B. Lan, M. Sun, L. Yu, *Front. Chem.* **2019**, *7*, 766.

- [33] Y. Wang, H. J. Yuan, F. Liu, T. J. Hu, *Chem. Commun.* **2021**, *57*, 2994–2997.
- [34] W. Peng, X. X. Yang, L. C. Mao, J. H. Jin, S. L. Yang, J. J. Zhang, G. Li, *Chem. Eng. J.* **2021**, *407*, 127157.
- [35] J. P. Xuan, H. B. Huang, J. J. Zhang, W. J. Dong, L. Yang, B. Wang, *J. Solid State Chem.* **2021**, *294*, 121788.
- [36] J. S. Liu, H. Zhang, J. S. Meng, C. H. Han, F. Liu, X. Liu, P. J. Wu, Z. A. Liu, X. P. Wang, L. Q. Mai, *ACS Appl. Mater. Interfaces* **2020**, *12*, 54545–54552.
- [37] J. Y. Qin, Z. W. Liu, D. Y. Wu, J. Yang, *Appl. Catal. B* **2020**, *278*, 119300.
- [38] T. J. Meng, A. Nsabimana, Z. Y. Liu, H. X. Jia, S. Y. An, H. Wang, Y. F. Zhang, *J. Colloid Interface Sci.* **2020**, *579*, 12–20.
- [39] J. N. Cai, X. F. Zhang, M. X. Yang, Y. D. Shi, W. K. Liu, S. Lin, *J. Power Sources* **2021**, *485*, 229251.

Submitted: February 16, 2023

Accepted: April 19, 2023